Characterization of Material Ductility of PP/EPR/talc Blend Under Wide Range of Stress Triaxiality at Intermediate and High Strain Rates

Hiroyuki Mae

Honda R&D Co., Ltd., 4630 Shimotakanezawa, Haga-machi, Haga-gun, Tochigi 321-3393, Japan

ABSTRACT: A ductile fracture locus formulated in the space of the effective plastic strain to fracture and the stress triaxiality for the polypropylene (PP) blended with ethylene-propylene rubber (EPR) and talc fillers is obtained at the intermediate and high strain rates by using a combined experimental-numerical approach. Biaxial loading tests on the flat butterfly specimens are carried out to characterize fracture behaviors under pure shear, combined shear and tension, pure tensile loading conditions at various loading velocities. Corresponding finite element analysis is performed to determine the evolution of stress, strain, and strain rate states. It is found that the material ductility strongly depends on the stress triaxiality for the present PP/EPR/talc blend. Meanwhile, the fracture surfa-

ces are observed by scanning electron microscopy, revealing that there exist two competing failure mechanisms: the multiple crazing at high positive stress triaxialities and void-sheeting like fracture mode at the low stress triaxiality. The transition of the failure modes occurs in the intermediate range of stress triaxialities. The obtained fracture locus covers a wide range of the stress triaxiality. It would be applicable to the fracture analysis of real automotive components such as interior or exterior polymeric components under various impact loading conditions. © 2008 Wiley Periodicals, Inc. J Appl Polym Sci 111: 854–868, 2009

Key words: mechanical properties; ductile; fracture; crazing; poly(propylene) (PP)

INTRODUCTION

Polypropylene (PP) toughened with elastomers and inorganic fillers has been found in wide applications to manufacture thin-walled components of intricate shape in automotive industries such as interior and exterior automotive parts. To improve the performance of PP/elastomer/filler components under overloading conditions such as collision, it is necessary to examine systematically material plasticity and fracture properties. At the same time, finite element (FE) analysis of the fracture response of PP/elastomer/filler components requires the quantification of those properties at the macroscopic level. This is the major objective of the present study.

The material ductility of PP toughened with elastomers and inorganic fillers were investigated in many researches.[1–6] Maerinrri and Ricco[1] prepared two particulate hybrid systems containing of PP with particles of ethylene-propylene rubber (EPR) and $CaCO_3$. It was investigated that the hybridization of the secondary phase produced the optimization of the impact fracture properties compared with

the corresponding binary systems. Premphet and Horanont[2] demonstrated the mechanical properties of PP/ethylene-octene copolymer/$CaCO_3$ and PP/ Ethylene-vinyl acetate/$CaCO_3$. Their results indicated the composites with separate dispersion of each phase showed higher modulus and impact strength than those of encapsulation type. Lehmann et al.[3] demonstrated that a combination of the grafted SiO_2 nanoparticles and elastomeric modifier was able to significantly increase the toughness of PP including the notch impact resistance although pregrafted nano-SiO_2 particles were not good enough to reduce the notch sensitivity of PP. Yang et al.[4,5] studied the phase structures and toughening mechanism in PP/EPDM (ethylene–propylene–diene monomer rubber)/SiO_2 composites. They blended hydrophilic SiO_2 nanoparticles with PP/EPDM composite by using two-step processing method, leading to a unique phase structure that EPDM particles are closely surrounded by nano-SiO_2 particles. This unique microstructure enhanced the Izod impact strength because the stress fields overlapped between EPDM and SiO_2 particles. Mae et al.[6] characterized the effect of SiO_2 nanoparticles on the mechanical properties of PP/SEBS (styrene ethylene butadiene styrene) blended with two types of SEBS particles whose particle diameters were different at the intermediate and high strain rates. On the basis

TABLE I
Detail of PP/EPR/talc Blend

	Weight ratio (%)	Volume ratio	Density (kg/m^3)	Molecular weight (g/mol)
PP	57	58.9	910	190,000
EPR	35	38.3	860	320,000
Talc	8	2.8	2700	–

of the results of the previous study, the location of SiO$_2$ nanoparticles was the most important parameters to increase the elastic modulus without decreasing the material ductility in the blend (PP/SEBS/ SiO$_2$) at both low and high strain rates.

Note, that those failure mechanisms were identified, all from the tensile tests or notched impact specimens, where the stress triaxiality ranged approximately larger than + 1/3. In contrast to those tensile failure mechanisms, the fracture mode of PP toughened with elastomers and inorganic fillers under shear and low stress triaxiality is less understood. The mechanical properties at the wide range of stress triaxiality of solid polymers were studied for constructing the yielding surface of polymer.[7,8] G'Sell et al. studied the effect of stress triaxiality on neck propagation of solid polymer.[9] However, these studies focused mainly on the yielding and necking behaviors, not on the fracture properties.

Then, in the present study, a ductile fracture locus formulated in the space of the effective plastic strain to fracture and the stress triaxiality for PP/EPR/talc blend is obtained using a combined experimental-numerical approach. The biaxial loading tests are conducted on the butterfly specimens at the three different deformation rates. The material coefficients of the elastoviscoplastic constitutive law are identified and the fracture locus is calibrated to characterize the plasticity and ductility of the PP/EPR/talc blend. Meanwhile, a fractographic examination on the butterfly specimens is performed to understand the microscopic failure mechanisms under a wide range of stress states at the intermediate and high strain rates.

SPECIMEN PREPARATION AND TEST PROCEDURE

Material and specimen preparation

Isotactic PP whose molecular weight was about 190,000 g/mol was used as the matrix polymer in this study. The density of PP was 900 kg/m^3. The blended elastomer was EPR, whose molecular weight was 320,000 g/mol and blend ratio was 35 wt %. The talc was blended at the blend ratio of 8 wt %. The present PP/EPR/talc blend had a melt flow rate = 30 g/10 min (230°C). All constitutes were purchased

from Prime Polymer, Japan. Detail of the present PP/ EPR/talc blend is shown in Table I. The mixed pellet was melted and injected into the molder. The injecting temperature was kept at 230°C during the manufacturing process. In the previous studies, the present PP/EPR/talc blend was also successfully applied to the microporous foaming.[10–12]

Transmission electron microscope (TEM: JEOL JEM-200CX) operating at 200 keV was used to investigate the phase morphology. After staining of samples with OsO$_4$, ultra-thin sections were prepared by using an ultramicrotome equipped with a diamond knife. The samples for the investigation were taken from the plate specimen which was made by injection molding. Figure 1 shows the morphology of the representative PP/EPR/talc blend where the three-phase morphology is clearly seen. EPR particles are dispersed randomly in the PP matrix although EPR particles were elliptical shape whose long axis was parallel to the injection direction. The elliptical shape of elastomer particles was also obtained in the other elastomer blended PP produced by injection molding in the previous studies by the same author.[6,13–17] The mean approximate diameter of EPR was 0.7 μm based on the image analysis. In the image analysis, the commercial based software (Azo-kun, Asahi Kasei Engineering, Japan) was used. The rubber particles were approximated as a circle and then the diameter of each circle was collected manually in the software.

Figure 2 shows the schematic illustration of flat butterfly specimen. This type of specimens has a
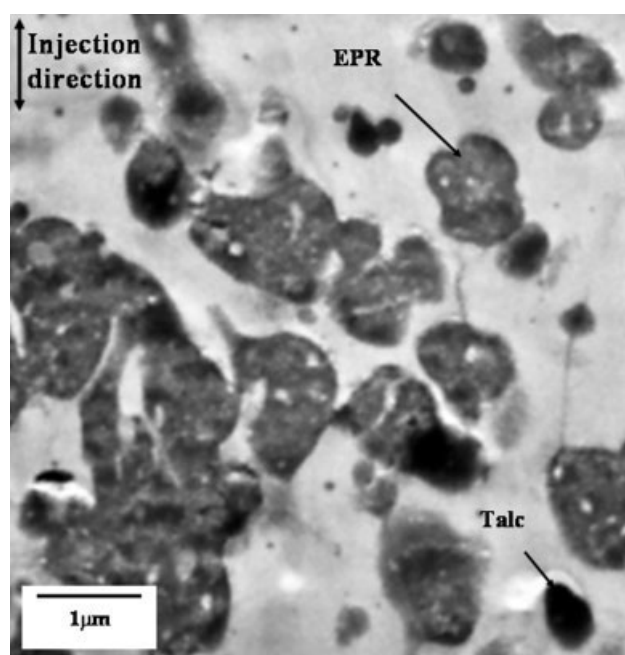

Figure 1 TEM morphological picture of the representative PP/EPR/talc blend.
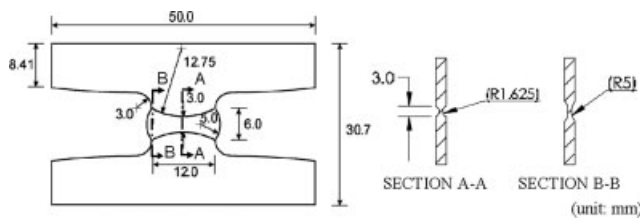
Figure 2 Schematic illustration of flat butterfly specimen.

complex, double curvature geometry in the gauge section. To ensure that a crack first occurs at the center of the gauge section, the central region has the minimal thickness of 1.0 mm, much smaller than the thickness of the shoulder region 3.0 mm. This is an advantage over conventional flat specimens, in which a crack is often generated at the boundary, particularly under shear. To hold the specimen securely, two long shoulders are designed to provide sufficient gripping area. This new type of flat specimens was first developed by Bao et al.[18,19] and was successfully used to calibrate the fracture properties of A710 steel, 2024-T351 aluminum alloy. In addition, this type of specimen was successfully applied to other materials such as various cast aluminum alloys by Mae et al.[20–25]

Actually, it is difficult to determine directly from the experiments whether fracture starts from the middle of the cross-section or from the surfaces. In other words, the experiments only explicitly give the location of crack initiation in the main plane but not in the thickness direction. The strain gradient through the thickness is small (the difference of strain between the middle of thickness and surface is less than 5%) due to the small thickness of the gauge section of the specimen. However, the difference of the stress triaxiality is not negligible and in fact about 20% between those two locations. Therefore, the exact location of crack formation was determined from numerical simulations by checking all the elements located at the center of the gauge section from the middle of thickness to the surface. In addition, it is likely that the crack initiates at the location with the highest stress triaxiality because the strain gradient through the thickness is small.

Biaxial loading tests on butterfly specimens

To construct an empirical fracture locus that covers a wide range of stress states, one has to carefully design specimen and experimental procedures. Generally, for obtaining the information on the fracture properties under tension, represented by high positive stress triaxialities, conventional tensile tests are conducted on notched and un-notched tensile test specimens. On the contrary, in the present study, the biaxial loading tests were conducted on the flat butterfly-like specimens. The effective plastic strains to fracture in the range of 0, low and high stress triaxialities were obtained from the biaxial loading experiments.

The biaxial tests on the butterfly specimens were carried out with a servo-hydraulic high-speed impact test apparatus (Shimazu EHF U2H-20L: maximum tensile speed 15 m/s). Figure 3 illustrates a
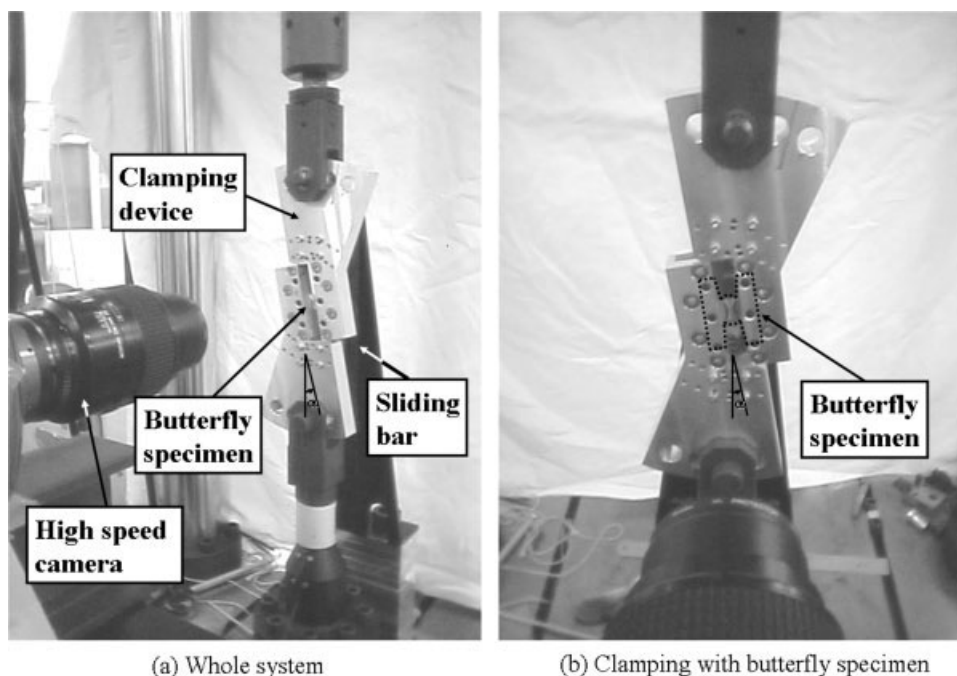

(a) Whole system

(b) Clamping with butterfly specimen

Figure 3 Butterfly specimen mounted in the clamping device with the orientation angle $\alpha = 10^{o}$.

flat butterfly specimen mounted in the clamping device with the orientation angle $\alpha = 10°$. By suitably changing the orientation of the specimen with respect to the loading direction, different stress states would develop from pure tension, combined tension and shear, all the way to pure shear. With this test method, one would be able to construct a fracture locus in a wide range of stress triaxialities, using one type of specimens.

The butterfly specimen is attached to the clamping device with the sliding table as shown in Figure 3, keeping the loading angle constant during the whole testing process. In the present tests, the clamping device was prescribed with the velocities of 0.013, 0.13, and 0.26 m/s, respectively. The vertical reaction forces of the specimens were measured by a load cell. The deformation process of the specimens was recorded by an optical measurement system, which included one high-speed camera (Phantom version 7.3, Vision Research), a digital photo acquisition device (Phantom, Memory: 4096 MB), and a postprocessing software (Phantom, Camera Control). The relative displacement of two points on the exterior surface of specimens can be calculated from images captured by the high-speed camera using the postprocessing software. The optical displacement measurement system and the servo-hydraulic loading system were synchronized and, thus, the relationship between the load and the displacement could be easily established. The frame rate of the high-speed video camera was 23,300 frames per second with the image resolution 256 × 512 pixels.

In the present study, 17 butterfly specimens were machined from the thin plate whose thickness was 3.6 mm produced by the injection molding. Four loading conditions were considered from pure shear to combined shear and tension. The orientation angles of the specimens were $\alpha = 0°$, 10°, 20°, 30°, and 90°, respectively. Two pure shear tests at the deformation velocity of 0.26 m/s and two combined shear and tensile tests at the deformation rate of 0.13 m/s were performed to examine the repeatability of experimental data.

CALIBRATION PROCEDURE OF PLASTICITY AND FRACTURE PROPERTIES

Finite element simulation

It was postulated that fracture is governed by the local stresses, strains, and their histories. However, it is very difficult or even impossible to determine individual components of stress and strain tensors at the location of fracture directly from the physical experiments, which brings the FE analysis to the present study.

Corresponding numerical simulations of all the tests were performed using a commercial explicit FE code, RADIOSS[26–29] version 4.4, to obtain individual components of stress and strain tensors at the location of fracture. RADIOSS is being developed by Altair Engineering Inc.[30] This code is based on the explicit time integration FE method and used for structural crash impact problem widely in the world. The FE method is based on the explicit scheme which used the central difference time integration. With this method, highly nonlinear problems, namely, contact, material plasticity, and large deformation, can be treated. The specimen was modeled as eight-node brick reduced integration elements (see Fig. 4). The total element number was 39,760. The finest elements of 0.1 mm × 0.1 mm × 0.1 mm were located in the central region of the gauge section. Each butterfly specimen was fixed in the grip area of the lower shoulder and is subjected to a vertical displacement in the grip area of the upper shoulder (see Fig. 5).

Elastoviscoplastic constitutive law with craze nucleation and growth

FE analyses were carried out by using RADIOSS version 4.4 with the user-defined material subroutine
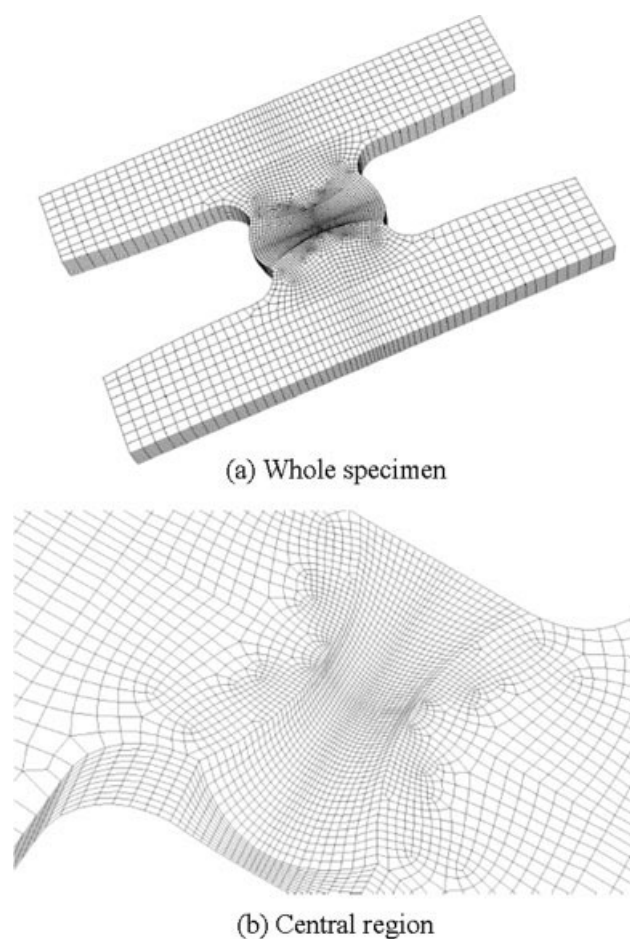

(a) Whole specimen

(b) Central region

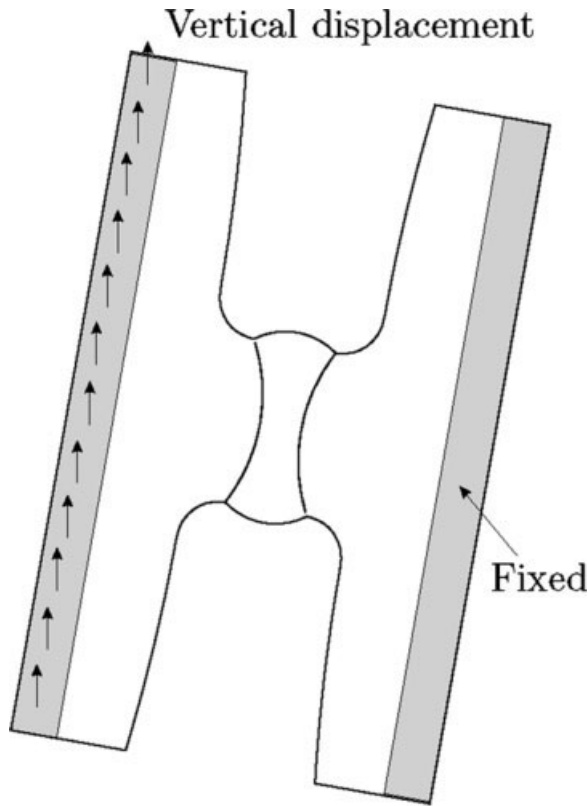**Figure 4** Finite element model of the butterfly specimen.

Figure 5 Schematic illustration of boundary conditions of the butterfly specimen. The grip area is shaded.

program developed for predicting the craze nucleation and growth of PP blends in the previous studies[31–34] while there has been considerable amount of work concerning the modeling of elastoviscoplastic-damage behavior of polymers.[35–38] RADIOSS offers the way to introduce an advanced material model into a numerical scheme through user-defined subroutine: User Material Laws. Two subroutines for one material model had to be developed for RADIOSS STARTER and RADIOSS ENGINE, respectively. The STARTER subroutine is used to initiate material parameters for the present material model. The ENGINE subroutine is applied to calculate damage accumulation based on the formation of the implemented material models described below. The more detail description can be found in Ref. 38

The proposed elastoviscoplastic constitutive equation with craze effect[31,32] is given by;

$$\overset{\triangledown}{\mathbf{T}} = \mathbf{C}^v : \mathbf{D} - \dot{\bar{\varepsilon}}^p (\cos\delta)\mathbf{P}' - \dot{\omega}\mathbf{T}/(1-\omega), \quad (1)$$

where $\mathbf{T}$ is Cauchy stress, $\mathbf{D}$ is deformation rate, $\dot{\bar{\varepsilon}}^p$ is equivalent plastic strain rate, ω is craze density, $\dot{\omega}$ is craze density rate and $(\triangledown)$ is Jaumann rate. $\mathbf{C}^v$, $\mathbf{P}'$, and $\cos\delta$ are defined in the following equations;

$$\mathbf{C}^v \equiv H_\omega(1-\omega)/(H_\omega + 3\mu)[\mathbf{C}^e + 3\mu/H$$
$$\times \{(3\lambda + 2\mu)/3\mathbf{I} \otimes \mathbf{I} + 3\mu\mathbf{T}' \otimes \mathbf{T}'/\bar{\sigma}^2\}], \quad (2)$$

$$\mathbf{P}' \equiv \mathbf{C}^v : \mathbf{m}' = 3\mu(1-\omega)\mathbf{T}'/\bar{\sigma}, \quad \mathbf{m}' \equiv 3/2\mathbf{T}'/\bar{\sigma}, \quad (3)$$

$$H_\omega \equiv 1/(1-\omega)\bar{\sigma}/(\dot{\bar{\varepsilon}}^p k), \quad \bar{\sigma} \equiv \left(3\overset{\triangledown}{\mathbf{T}}' \cdot \overset{\triangledown}{\mathbf{T}}'/2\right)^{1/2}, \quad (4)$$

$$\cos\delta = (1 - \sin^2\delta)^{12}, \quad \sin\delta = k(m)\sin\alpha, \quad (5)$$

where $\mathbf{m}'$ is stress direction tensor, m is the strain rate sensitivity parameter and $\cos\alpha$ is defined as

$$\cos\alpha \equiv \mathbf{T}' \cdot \overset{\triangledown}{\mathbf{T}}'(\mathbf{T}' \cdot \mathbf{T}')^{-1/2}\left(\overset{\triangledown}{\mathbf{T}}' \cdot \overset{\triangledown}{\mathbf{T}}'\right)^{-1/2}. \quad (6)$$

As suggested by Kobayashi et al.,[33] the craze evolution equation is written as follows;

$$\dot{\omega} = A(1-\omega)\langle\dot{\varepsilon}_m^p\rangle$$
$$+ 1/2BD_1^{\dot{\bar{\varepsilon}}^p}[1 + \tanh\{-D_2(\bar{\varepsilon}^p - \varepsilon_c)\}], \dot{\bar{\varepsilon}}^p, \quad (7)$$

where A, B, D_1, and D_2 are material constants. $\dot{\varepsilon}_m^p$ is the mean normal plastic strain rate defined as

$$\dot{\varepsilon}_m^p = \{(q_1\omega)\cosh((q_2\omega + q_3)\sigma_m/\sigma_y)\}, \quad (8)$$

where σ_m is the hydrostatic stress, σ_y is the yield stress, q_1–q_3 are material constants. The first part of eq. (7) means craze evolution depending on the normal plastic strain rate. The $BD_1^{\dot{\bar{\varepsilon}}^p}$ in the second term of eq. (7) means that the craze growth gets larger at the lower strain rate. The rest of the second term of eq. (7) characterizes that the craze stops growing with the strain hardening.[33] Then, ε_c is the strain at which the craze stops growing. The craze generation is based on the hydrostatic stress criterion as eq. (9);

$$\sigma_b \geq A_1 + (B_1/3\sigma_m) \quad \sigma_b = \sigma_1 - v\sigma_2 - v\sigma_3, \quad (9)$$

in which σ_b is the stress needed for fibril orientation, σ_m is the hydrostatic stress, σ_1–σ_3 are the principal stresses, A_1 and B_1 are material constants.

With strain rate dependent coefficient m, the strain hardening equation is modeled in the following equations;

$$\dot{\bar{\varepsilon}}^p = \dot{\varepsilon}_r|\bar{\sigma}/g(\bar{\varepsilon}^p)|^{1/m}, \quad (10)$$

$$g(\bar{\varepsilon}^p) = \sigma_r\{\tanh(k_1\bar{\varepsilon}^p) + k_2 + H_e(\bar{\varepsilon}^p - \varepsilon_r)$$
$$k_3(\exp\bar{\varepsilon}^p - \exp\varepsilon_r)\}, \quad (11)$$

where $\bar{\sigma}$ is the equivalent stress, $g(\bar{\varepsilon}^p)$ is the flow stress modeled for PP, $\dot{\varepsilon}_r$ is the reference strain rate, σ_r is the reference stress, ε_r is the reference strain at which the second hardening begins. k_1–k_3 are

Step 1. Smooth specimen up to 2 mm

$$\boxed{\sigma_r \; k_1 \; k_2 \; k_3 \; m}$$

Step 2. Notched specimen before failure

$$\boxed{B \; A_1 \; D_1}$$

Step 3. Smooth specimen before failure

$$\boxed{\varepsilon_c \; \sigma_y \; q_3}$$

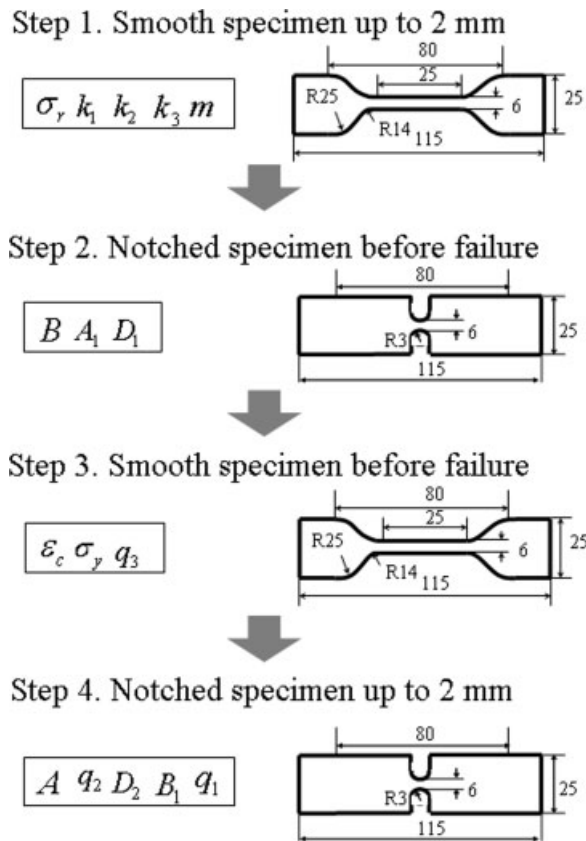Step 4. Notched specimen up to 2 mm

$$\boxed{A \; q_2 \; D_2 \; B_1 \; q_1}$$

Figure 6 Material parameter identification procedure.

material constants. $H_e(x)$ is the following step function.

$$H_e(x) = 1 \;(\text{at } x > 0), \quad 0 \;(\text{at } x < 0). \tag{12}$$

The material coefficients need to be first determined from the tests. This task is not trivial and still imposes a challenge. Several approaches were suggested in the literature. For example, Zhang et al. proposed a practical method to calibrate the true stress-strain curve for flat specimens up to localized necking.[40] This approach is not applicable to the present case with fracture, especially because of the biaxial loading tests on the butterfly specimens. In the previous study, the procedure for the material parameter identification in the present constitutive law was developed based on the parameter sensitivity analyses.[34] In this procedure, all material parameters could be identified by using the load-displacement histories of a smooth tensile specimen together with a notched tensile specimen under uniaxial tensile loading. Figure 6 shows the material parameter identification procedure constructed by the previous study.[34,41] In each step, the corresponding FE analyses were conducted at the nominal tensile strain rates of 1, 10, and 100 s^{-1}, where the material coefficients were identified so that the simulated

TABLE II
Material Coefficients for Finite Element Analysis with Elastic Modulus E = 800 MPa and Poisson's Ratio μ = 0.41

A	0.192	σ_r	10.055 (MPa)
B	0.613	σ_y	17.432 (MPa)
A_1	1.982 (MPa)	k_1	44.795
B_1	417.665 (MPa $\times$ MPa)	k_2	0.863
D_1	0.999	k_3	1.243
D_2	100.541	q_1	0.0001177
ε_c	1.087	q_2	12.44
m	0.069	q_3	2.908
$\dot{\varepsilon}_\gamma$	1 (s^{-1})	ε_r	0.0001

load-displacement histories could agree with the experimental results in each strain rate. Here, ε_r and $\dot{\varepsilon}_r$ were fixed as 1 s^{-1} and 0.0001, respectively, because they were the reference values. The strain-rate sensitivity parameter m was identified by the early stage of the load-displacement curves at the three different strain rates. The effect of the stress triaxiality was considered by using the experimental data obtained from the notched tensile test specimens. With these identified parameters, the predicted load-displacement histories were validated in both the dart impact test mode and the impact test of the actual automotive polymeric component.[41] In this study, the same material coefficients identified in the previous study[33] were used except for the parameters of craze evolution law which were readjusted slightly from the previously identified parameters by forcing a numerically predicted load-displacement curve of the butterfly specimen to match more closely experimental data. The material constants used in the present study are shown in Table II.

MATERIAL PLASTICITY AND FRACTURE PROPERTIES

True stress strain curves

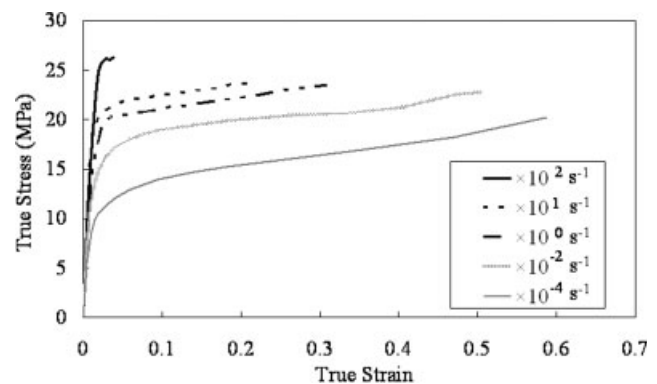Figure 7 shows the true stress strain curves at wide range of strain rates obtained in the previous

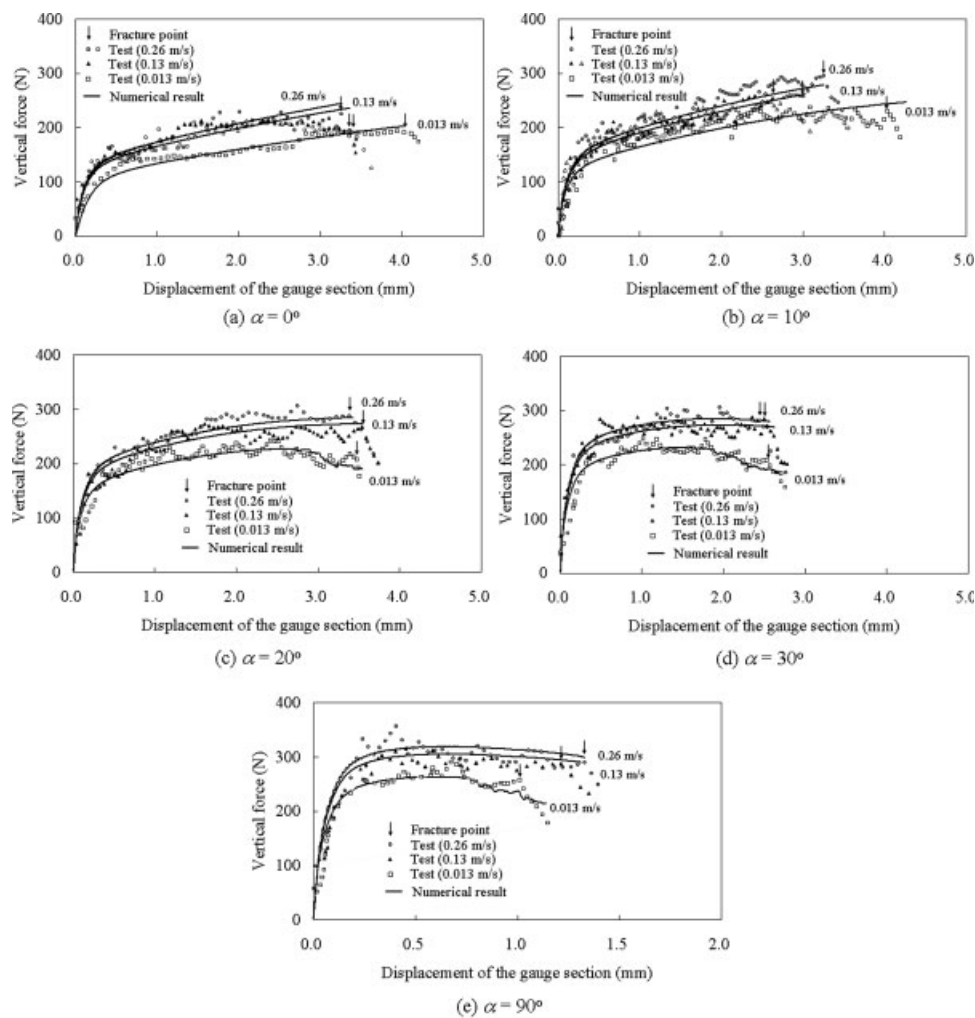**Figure 7** True stress strain curves at wide range of strain rates.

Figure 8 Load-displacement curves obtained from the butterfly specimens at various vertical velocities.

study.[34,41] In the previous studies,[33,41] the dumbbell-shape smooth tensile specimens (Japanese Industrial Standard K713, No. 2) with the parallel portion width of 6 mm and the thickness of 3.6 mm were used. Note, that the in-plane deformation of the test specimen was recorded during the tensile test to measure the longitudinal strain and the lateral strain by using a high-speed video camera. The incompressibility of the materials was assumed for large deformation to obtain the true stress by simple calculation. The ratio of the longitudinal strain and the lateral strain under larger deformations was estimated as about −0.46. Thus, it is considered that the estimated true stress was in the error range of several percentages. The strain rate was calculated by the gauge length and the tensile velocity, which means that the present strain rate was the nominal strain rate. However, the material parameters of the present constitutive law were identified directly from the load-displacement curves of the tensile tests. Thus, the strain rates shown in Figure 7, were not used for the parameter identification in this study. As shown in Figure 7, it

was clearly observed that the present PP/EPR/talc blend had the strong strain rate dependency.

Load-displacement responses

Figure 8 shows the global load-displacement curves for 17 tests. It appeared that the numerical predictions had good correlation with experimental results. This validated that the materials constants were reasonably identified in the present study. In every loading angle, the vertical reaction forces gradually increased, reached the plateaus (or gradually decreased), and then decreased drastically with the prescribed displacement as the cracks were growing in a stable way. In addition, the load levels increased as the vertical velocity went up because of the viscoplasticity of the present PP/EPR/talc blend. The loading plateau or the gradual decrease of load indicated that plastic deformation was fully developed in the central region of the specimen before fracture, leading to the highly growing crazes. The load drop was identified as the instant at the point of fracture
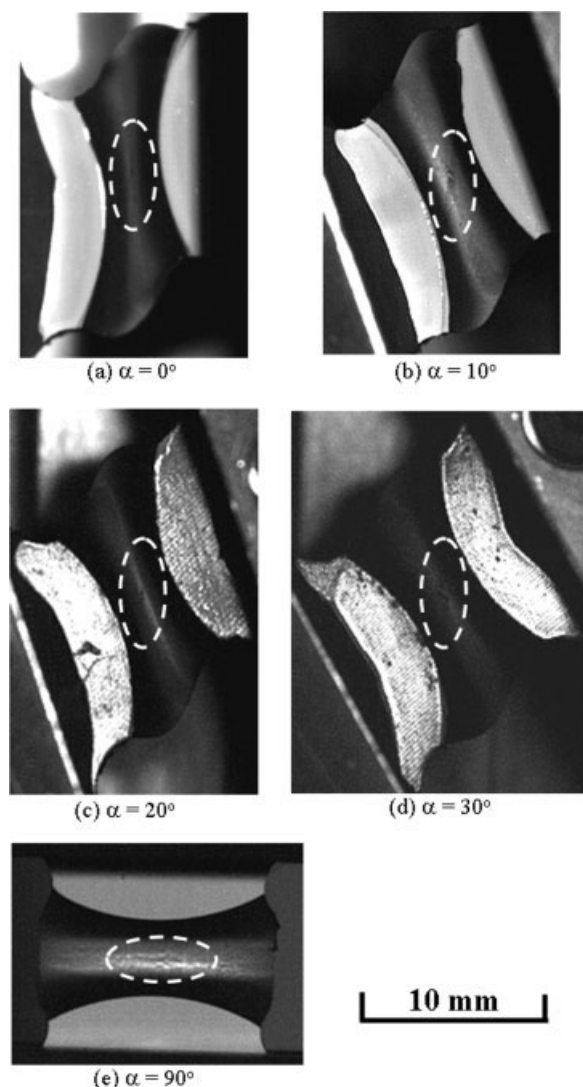
Figure 9 Pictures of the butterfly specimens obtained by high-speed camera at the vertical displacement rate of 0.26 m/s. The white-color circles indicate the crack formation site.

in the present study. On the basis of the images obtained by the high-speed video camera at the point of fracture, the cracks were always found on the outer surface in the central region of the gauge section (see Fig. 9). Figure 9 illustrates the gauge section which was the central portion between the white-color areas painted on the boundary of the two curvatures ($R = 12.75$ mm) at the vertical velocity of 0.26 m/s. The instants of fracture are marked by the vertical arrows in Figure 8, and used to calibrate the fracture locus of the present PP/EPR/talc blend.

To examine experimental repeatability, the shear tests at the vertical velocity of 0.26 m/s and the combined shear and tensile tests at the vertical velocity of 0.13 m/s were performed twice in this

research. It appears from Figure 8 that the load-displacement curves were generally close to each other.

Ductile fracture locus

In this study, the ductility is understood as an intrinsic ability of a material to undergo a certain amount of plastic deformation without the occurrence of macroscopic cracks. A number of fracture criteria have been developed in the literature to describe the ductility. Wierzbicki et al. critically examined seven ductile fracture models commonly adopted in practical applications.[42–44] They pointed out that a fracture locus formulated in the space of the effective plastic strain to fracture and the stress triaxiality would be the most suitable for a variety of problems while the fracture properties can be also analyzed in term of stresses. In the present study, the fracture properties were investigated in term of strain because the strain-based fracture model was more applicable to the practical applications such as the crash explicit FE simulation. A general form of the strain-based fracture loci can be written as

$$\bar{\varepsilon}_f = f(\eta) = f\left(\frac{\sigma_h}{\bar{\sigma}}\right), \qquad (13)$$

where $\bar{\varepsilon}_f$ is the effective plastic strain to fracture, η is the stress triaxiality defined by the ratio of the hydrostatic stress σ_h to the equivalent stress $\bar{\sigma}$. The major task of this section is to determine the explicit expressions of eq. (13) for the present PP/EPR/talc blend.

By combining the fracture tests with the corresponding FE analysis, one would be able to construct an empirical fracture locus in the space of the stress triaxiality and the effective plastic strain to fracture. The numerical simulations provide the evolution of stress, strain, and strain rate states at each material point. The instants at the point of fracture were determined from the fracture tests in the form of the critical displacement of the gauge section. Figure 10 shows the simulated stress triaxiality and craze density distributions right after the point of fracture for loading angle $\alpha = 10°$ with the displacement rate of 0.13 m/s. The numerical simulation successfully captured the highly localized deformation at the gauge section and also the deformed shape of edge curvatures. As shown clearly, the largest stress triaxiality was distributed at the central portion of the gauge section, leading to the highest craze density at the center of the gauge section. Indeed, the correlations between experiments and numerical simulations were very good in terms of deformed shape of the butterfly specimen, in addition to the load-displacement responses.
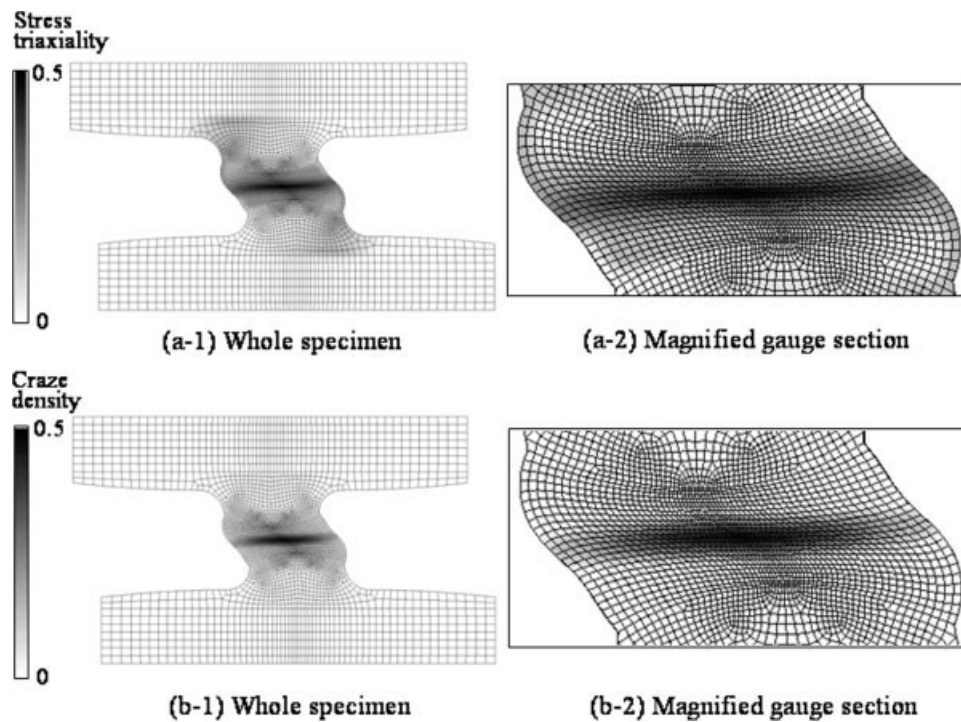
Figure 10   Deformed specimens with distributions of stress triaxiality and craze density under 10° loading at 0.13 m/s.

Figure 11 shows the comparison of the stress triaxialities (and equivalent plastic strain rate) of the material points at the external surface and the middle thickness of the central position of the gauge section when the loading angle was 10° at the vertical displacement rate of 0.13 m/s. As shown clearly, the stress triaxiality of the middle thickness was larger than that of the external surface at the beginning of the deformation process. In the brittle materials, it can be assumed that the crack usually should first occur in the middle thickness of the gauge section because the deformation up to failure was relatively small. On the contrary, in the case of ductile materials such as the present PP/EPR/talc blend, it is expected that the first crack formation site could be the external surface at the center of the gauge section because the stress triaxiality of the external surface became larger than that of the middle thickness when the displacement of the gauge section reached 0.8 mm as shown in Figure 11. The equivalent plastic strain rate of the external surface was a little larger than the middle thickness. Therefore, in the present study, the material point at the external surface of the central location of the gauge section was identified as the critical sites for the onset of fracture. Their stress, strain, and strain rate states were used to calibrate the fracture locus, which was different from the critical location in the case of cast aluminum alloys in the previous studies.[20–25]

Figure 12 shows the evolutions of the stress triaxiality and the effective plastic strain of the critical

points up to fracture at the vertical displacement rates of 0.013, 0.13, and 0.26 m/s, respectively. To represent the stress state of the critical points during the whole loading process, an average value of the stress triaxiality for each loading angle and each vertical velocity was defined in the range from 0 to $\bar{\varepsilon}_f$:

$$\left(\frac{\sigma_h}{\bar{\sigma}}\right)_{av} = \frac{1}{\bar{\varepsilon}_f} \int_0^{\bar{\varepsilon}_f} \frac{\sigma_h}{\bar{\sigma}} d\bar{\varepsilon}_{pl}. \tag{14}$$

The fracture strain $\bar{\varepsilon}_f$, determined from the numerical simulation, is the effective plastic strain corresponding to the measured displacement to
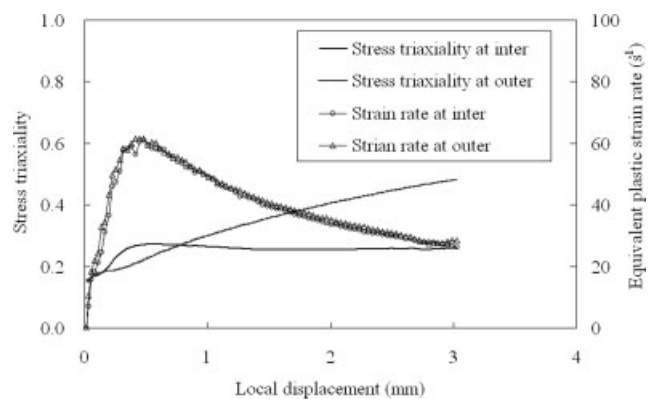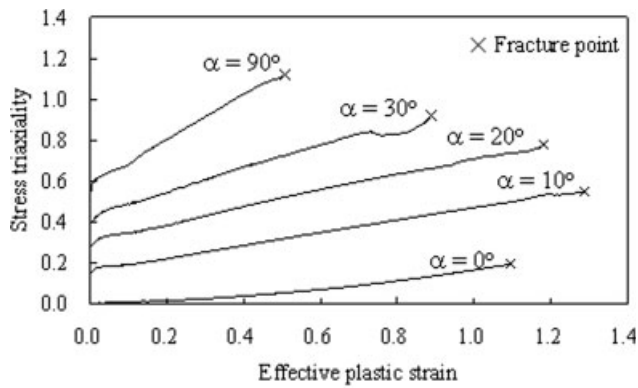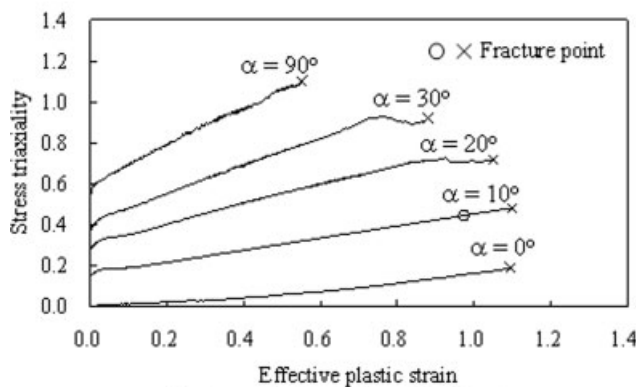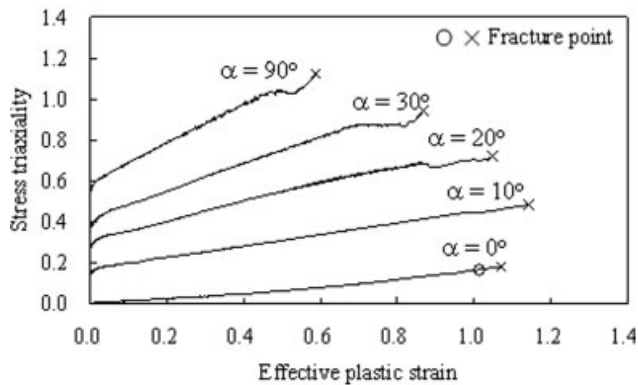

Figure 11   Stress triaxialities versus effective plastic strain of the material points at the external surface and the middle thickness of the central position of the gauge section when the loading angle was 10° at the vertical displacement rate of 0.13 m/s.

Figure 12 Evolutions of the stress triaxiality and the effective plastic strain of the critical points up to fracture at the vertical displacement rates of 0.013, 0.13, and 0.26 m/s.

fracture u_f. The stress triaxiality at the fracture can be used for the fracture locus. However, in this study, it was assumed that the fracture was a process of damage accumulation, in which the stress triaxiality changed with the plastic strain. Therefore, an average value of the stress triaxiality for each loading case was used to represent the stress state of the critical point (fracture point) during the whole loading history. This is apparent for very ductile materials. The damage accumulation was very im-

portant since the stress triaxialities in all these tests vary in a relatively narrow range, it is considered that the definition of the average value would not introduce large errors, which would be applicable for the practical engineering applications.
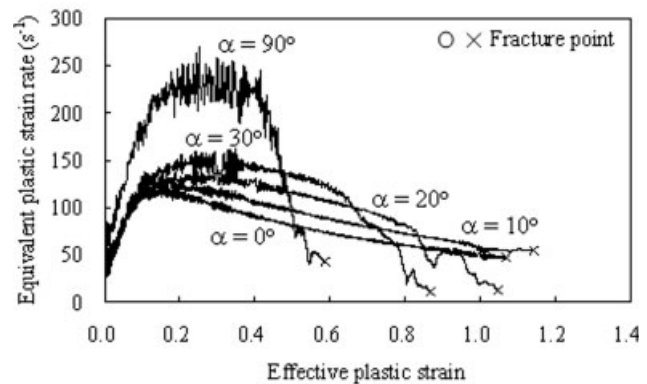
Figure 13 shows the equivalent plastic strain rate histories of the critical points up to failure at the vertical displacement rates of 0.013, and 0.13 and 0.26 m/s for every loading angle. Table III shows the mean equivalent plastic strain rate up to failure in various loading cases. As shown clearly, the
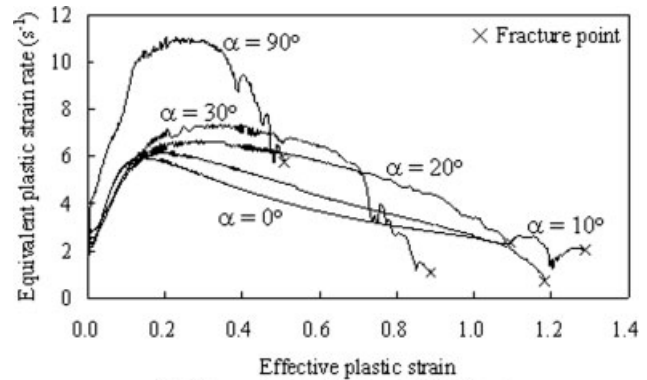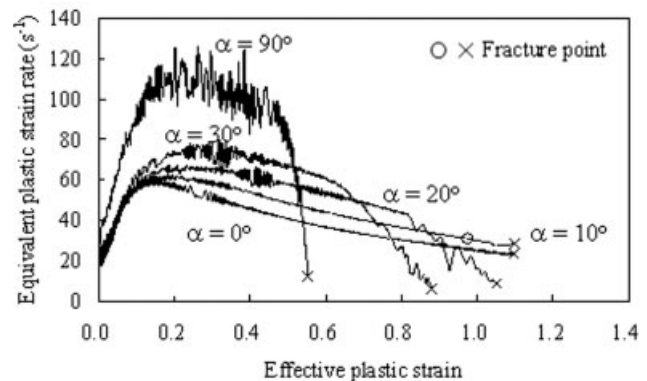
Figure 13 Equivalent plastic strain rate histories of the critical points up to failure at the vertical displacement rates of 0.013, 0.13, and 0.26 m/s for every loading angle.

TABLE III
Mean Equivalent Plastic Strain Rates (s^{-1})

Vertical velocity (m/s)	$\alpha = 0°$	$\alpha = 10°$	$\alpha = 20°$	$\alpha = 30°$	$\alpha = 90°$
0.013	3.54	3.45	4.02	4.00	7.88
0.13	34.99	41.46	38.53	41.95	76.50
0.26	71.36	78.60	71.06	78.50	127.51

equivalent plastic strain rates were approximately the same among every loading angles except for $\alpha = 90°$ although the vertical displacement rate was identical. This was because the strain at $\alpha = 90°$ was most highly localized among them.

For practical applications, it would be preferable to use an analytical curve to fit the fracture test data. Because the local equivalent plastic strain rate was not identical among every loading case, it was very difficult to construct the analytical fracture curve with the equivalent plastic strain rate term. Then, for simplicity, an attempt has been made for fitting all the fracture test data in this study, which means that the fracture test data at all vertical velocities would be fitted in one analytical curve without equivalent plastic strain rate term. In the range of high positive stress triaxialities, an exponential function is widely used to describe the effective plastic strain to fracture:

$$\overline{\varepsilon}_f = [C_1\exp(C_2\eta) + C_3], \quad \frac{1}{3} \leq \eta, \quad (15)$$

where C_1, C_2, and C_3 are three material coefficients and need to be determined from tests. This functional form was first developed by Rice and Tracey[45] by studying the enlargement of a spherical void embedded in a plastic matrix under hydrostatic tension, in which $C_2 = -1.5$ and $C_3 = 0.0$ were determined theoretically and C_1 was left for calibration. The applicability of eq. (15) has been checked by a number of round bar fracture tests on various metals,
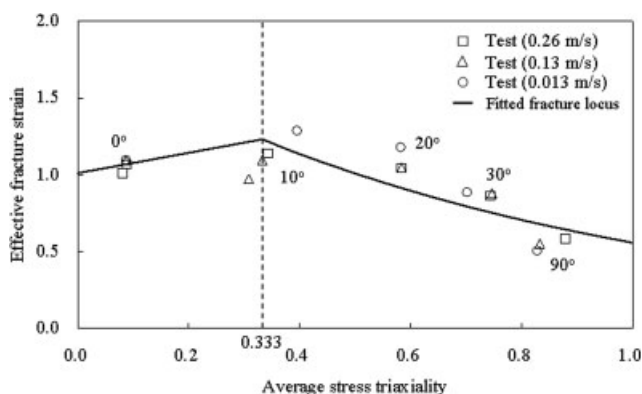
e.g., Hancock and Mackenzie[46] and Johnson and Cook.[47] The exponential function always gives an excellent fit to the experimental data. In this study, the exponential function was used for fitting the fracture strains at $\eta > +1/3$ because the calibrated ductility seemed to be well fitted for simplicity.

In the intermediate range from pure shear to the stress triaxiality of $+ 1/3$, a linear relationship between the effective fracture strain and the stress triaxiality is simply defined:

$$\overline{\varepsilon}_f = \lfloor \overline{\varepsilon}_{f,t} + (\overline{\varepsilon}_{f,t} - \overline{\varepsilon}_{f,s})(3\eta - 1) \rfloor, \quad 0 \leq \eta \leq \frac{1}{3}, \quad (16)$$

where $\overline{\varepsilon}_{f,t}$ is the effective fracture strain under uniaxial tension with $\eta = +1/3$, and $\overline{\varepsilon}_{f,s}$ is the effective fracture strain at $\eta = 0$. Here it is assumed that the transition of the failure mechanisms occurs at $\eta = +1/3$ and $\eta = 0$, which correspond to uniaxial tension and pure shear, respectively. Such a ductile fracture locus was first developed by Bao and Wierzbicki[42] based on a series of fracture experiments.

Each test provided a point in the space of the average stress triaxiality and the effective fracture strain, see Figure 14. C_1 and C_2 were optimized from all the biaxial loading test results in three vertical velocities with $C_3 = 0.0$. Table IV lists the detailed values of the parameters C_1 and C_2. It appears from Figure 14 that the material ductility sharply decreased with the increasing stress triaxiality above $+ 1/3$ at every vertical velocity. For instance, the effective fracture strain reached 1.10 at the stress triaxiality of 0.09 while the effective fracture strain was as low as 0.51 at the stress triaxiality of 0.83 at the vertical velocity of 0.013 m/s. The interesting result here was that the fracture strain increased slightly at the low stress triaxialities between 0 and $+ 1/3$. The similar trends such as the increase of fracture strain at the intermediate stress triaxiality were reported by Bao and Wierzbicki[17,42] on aluminum alloy A2024-T351 and steel A710, and Barsoum and Faleskog[48] on Weldox steel. It is considered that those trends might be caused by the shift of the fracture mechanism from shear to tensile loading.

Fractographic analysis

To better understand the failure mechanism of PP/EPR/talc blends under various loading conditions, the fracture surface of each specimen was examined

Figure 14   Fracture locus of PP/EPR/talc blend.

TABLE IV
Material Coefficients of Fracture Locus

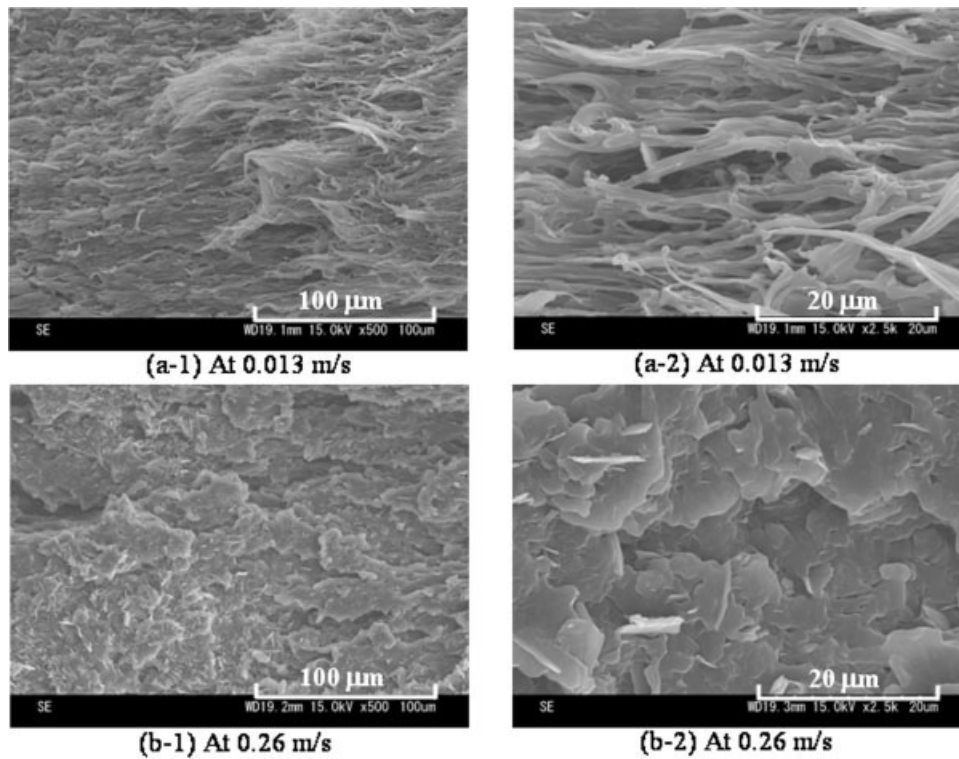| C_1	C_2	C_3
1.826	−1.185	0.0

Figure 15 Fractographs of the combined tension and shear tests with $\alpha = 20^o$ at the vertical velocities of 0.013 and 0.26 m/s.

with a scanning electron microscopy (SEM: HITA-CHI *S*-4300SE/N). Some of the SEM pictures are selectively presented in this article. Figures 15 and 16 show the fractographs under $\alpha = 20^o$ and 30° at the vertical velocities of 0.013 and 0.26 m/s. At both loading angles, a number of crazes, which were a
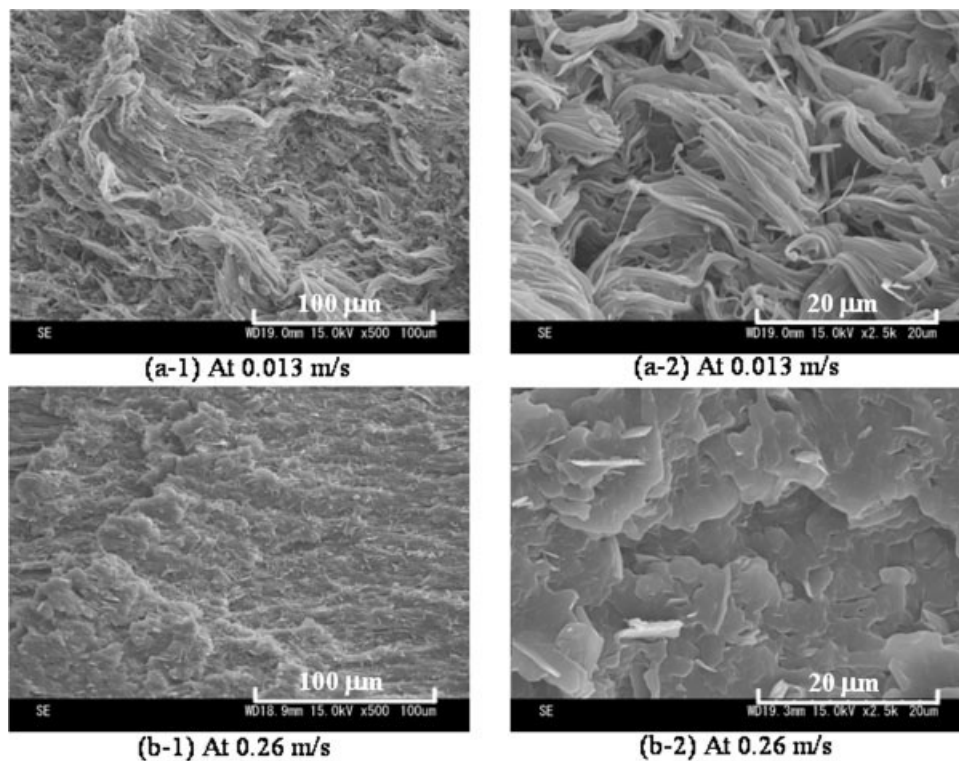

Figure 16 Fractographs of the combined tension and shear tests with $\alpha = 30^o$ at the vertical velocities of 0.013 and 0.26 m/s.
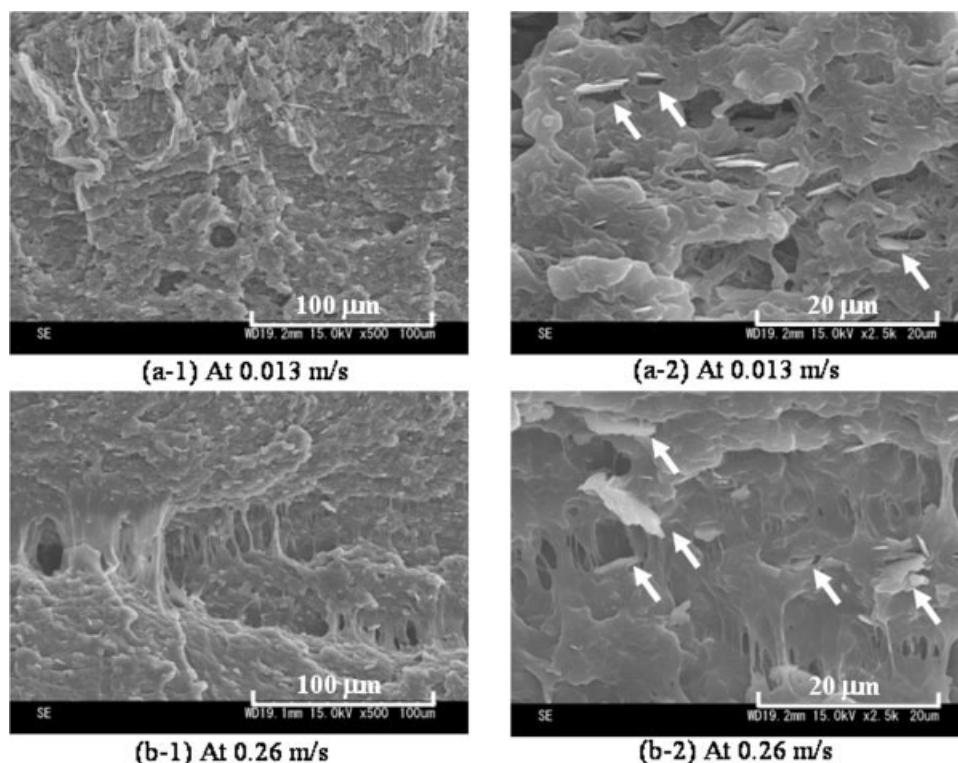
Figure 17 Fractographs of the pure tension with α = 90° at the vertical velocities of 0.013 and 0.26 m/s.

typical characteristic of the ductile fracture of PP/EPR/talc blend, can be easily recognized at the vertical velocities of 0.013 m/s. On the other hand, the fracture surfaces exhibited the smooth, flat area at the vertical velocities of 0.26 m/s, which were brittle fracture surfaces. The present PP/EPR/talc blends showed the rubber-glass phase transition at the nominal strain rate between 10 and 100 s^{-1} based on the tensile test results of the smooth tensile specimens in the previous study[34,41] (see Fig. 6). In addition, as shown in Table III, the present FE analysis indicated that the equivalent plastic strain rate would be in the rubber-glass phase transition strain rate, leading to that the brittle fracture mechanism was dominant at the vertical displacement rate of 0.26 m/s. According to Figure 14, the calibrated effective fracture strain was larger at 20° than 30° at the deformation rate of 0.013 m/s. The comparison between Figures 15(a) and 16(a) indicate that the elongated fibril structures were more highly oriented at 20° than 30°, which supports well the calibrated fracture strains.

On the contrary to the cases of α = 20° and 30°, the fracture surfaces at α = 90°, which was the highest stress triaxiality among all loading cases, showed the interesting result as shown in Figure 17. At this loading angle, the equivalent plastic strain rate was larger than those at other loading angles, leading to the partially brittle fracture surface even at the vertical velocity of 0.013 m/s [see Fig. 17 (a-1) and (a-2)].

This is the reason why the fracture strains at 90° were the smallest among all loading angles as shown in Figure 14. Moreover, the debonding can be clearly found in the interface between PP/EPR matrix and talc fillers indicated by white-color arrows in Figure 17. The reason why these debondings were clearly obtained at this loading angle was that the highest triaxial stress states would make the debonding between PP/EPR and talc more dominantly, leading to the highly cavitated fibril structures on the fracture surfaces as shown in Figure 17 (b-1) and (b-2). It is considered that this mechanism would keep the material ductility at the vertical velocity of 0.26 m/s similar to that at the vertical displacement rate of 0.013 m/s.

As the ratio of shear to tension increased, the elongation of the fibril structures along the shear direction became evident, see Figure 18 for the case with α = 10°. It is expected that this would correspond to the transition from the multiple crazing to the void-sheeting like fracture mode. The calibrated fracture strains at this loading angle were the largest, indicating that the mixed fracture mode of the crazing and void-sheeting like fractures would enhance the material ductility.

The pure shear tests gave the distinct fracture surfaces from the positive stress triaxialities. It can be seen from Figure 19 that the crazes were much smaller and shallower under shear than under low stress triaxialities. The fracture surfaces were
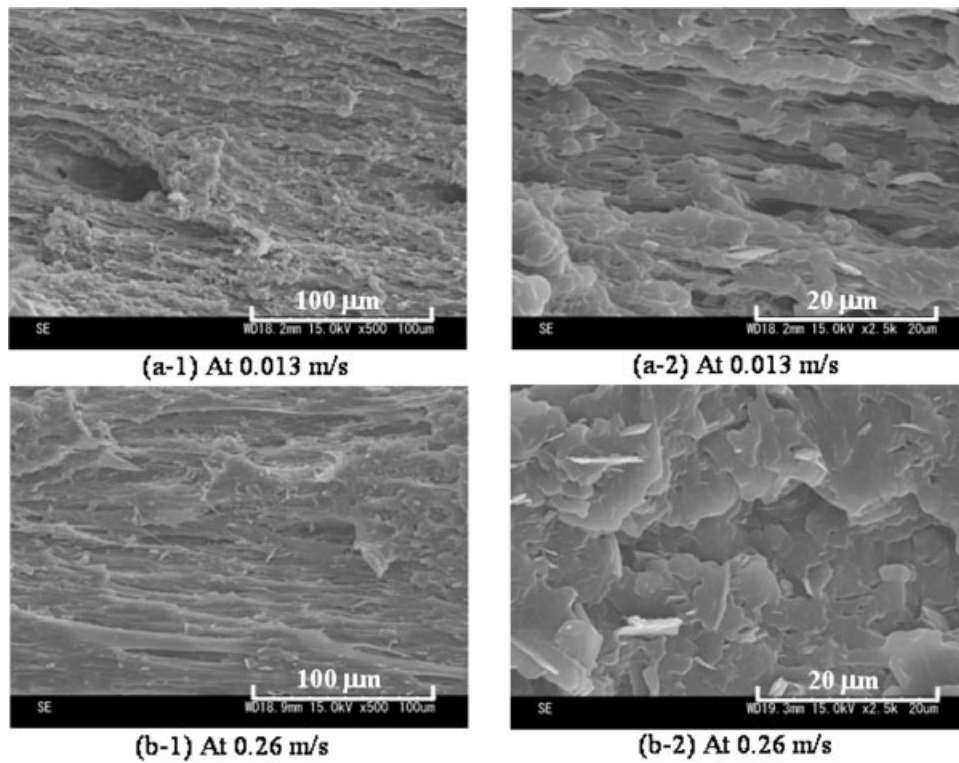
Figure 18 Fractographs of the combined tension and shear tests with $\alpha = 10^\circ$ at the vertical velocities of 0.013 and 0.26 m/s.

relatively smooth. Moreover, the difference between Figure 19(a, b) was quite small. On the other hand, the calibrated fracture strains were similar at all dis-

placement rates at the loading angle of 0°, supporting the presently observed fracture surfaces. It is not clear how small cracks developed between primary
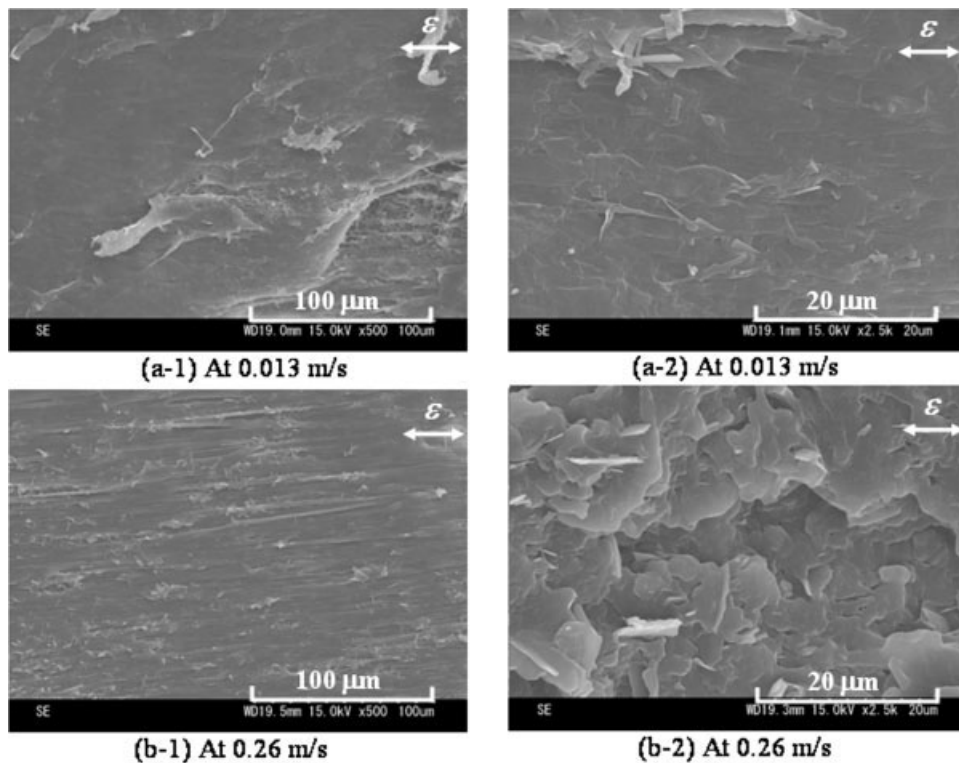

Figure 19 Fractographs of the simple shear tests with $\alpha = 0^\circ$ at the vertical velocities of 0.013 and 0.26 m/s.

small crazing sites leading to the relatively smooth fracture surface at this range of the stress triaxiality. Compared to the tensile failure, the fracture mechanism under shear is less understood. The problem needs to be further explored in the future study.

CONCLUSIONS

In this article, ductile fracture properties of PP/EPR/talc blend were characterized in the form of a fracture locus using a combined experimental-numerical approach. The butterfly specimens were tested to fracture under a wide range of stress states including pure tension, combined tension and shear, and pure shear. To describe the plasticity and ductility of PP/EPR/talc blend, the material coefficient of the elastoviscoplastic constitutive law with craze nucleation and growth, and the fracture locus were calibrated, respectively, from the experimental data in combination with the FE analysis.

The ductile fracture locus was formulated in the space of the effective plastic strain to fracture and the stress triaxiality. It appears that there is a very strong dependency of the material ductility of the stress triaxiality. The effective fracture strain reached 1.10 at the stress triaxiality of 0.09 whereas the effective fracture strain was as low as 0.51 at the stress triaxiality of 0.83 at the vertical velocity of 0.013 m/s.

The obtained fracture locus covers a wide range of the stress triaxiality. It would be applicable to the fracture analysis of real automotive interior or exterior components under various loading conditions.

References

1. Maerinrri, F.; Ricco, T. J Mater Sci 1994, 29, 442.
2. Premphet, K.; Horanont, P. J Appl Polym Sci 2000, 76, 1929.
3. Lehmann, B.; Friedrich, K.; Wu, C. L.; Zhang, M. Q.; Rong, M. Z. J Mater Sci Lett 2003, 22, 1027.
4. Yang, H.; Zhang, Q.; Guo, M.; Wang, C.; Du, R. N.; Fu, Q. Polymer 2006, 47, 2106.
5. Yang, H.; Zhang, X.; Qu, C.; Li, B.; Zhang, L.; Zhang, Q.; Fu, Q. Polymer 2007, 48, 860.
6. Mae, H.; Omiya, M.; Kishimoto, K. J Solid Mech Mater Eng 2008, 2, 254.
7. Pae, K. D. J Mater Sci 1977, 12, 1209.
8. Lu, M. L.; Chiou, K. C.; Chang, F. C. J Polym Res 1996, 3, 73.
9. G'Sell, C.; Aly-Helal, N. A.; Jonas, J. J. J Mater Sci 1983, 18, 1731.
10. Mae, H.; Omiya, M.; Kishimoto, K. Mater Sci Eng A 2008, 477, 168.
11. Mae, H. Mater Sci Eng A 2008, 496, 455.
12. Mae, H.; Omiya, M.; Kishimoto, K. J Solid Mech Mater Eng 2008, 2, 616.
13. Mae, H.; Omiya, M.; Kishimoto, K. J Appl Polym Sci 2008, 107, 3520.
14. Mae, H.; Omiya, M.; Kishimoto, K. Int J Modern Phys B 2008, 22, 1129.
15. Mae, H.; Omiya, M.; Kishimoto, K. J. Soc Mater Sci Japan 2008, 57, 951.
16. Mae, H.; Omiya, M.; Kishimoto, K. J Appl Polym Sci 2008, now is early view status.
17. Mae, H.; Omiya, M.; Kishimoto, K. J Appl Polym Sci 2008, 110, 1145.
18. Bao, Y.; Bai, Y.; Wierzbicki, T.; Tech Report No. 135, Impact Crashworthiness Lab, MIT: Cambridge, MA, 2005.
19. Wierzbicki, T.; Bao, Y.; Bai, Y.; Proc 2005 SEM Annu Conf Exposition Appl Mech, 1295.
20. Mae, H.; Teng, X.; Bai, Y.; Wierzbicki, T. Mater Sci Eng A 2007, 459, 156.
21. Mae, H.; Teng, X.; Bai, Y.; Wierzbicki, T. Int J Solids Struct 2008, 45, 1430.
22. Mae, H.; Teng, X.; Bai, Y.; Wierzbicki, T. J Jpn Soc Exp Mech 2008, 8, 45.
23. Mae, H.; Teng, X.; Bai, Y.; Wierzbicki, T. J. Soc Mater Sci Jpn 2008, 57, 913.
24. Mae, H.; Teng, X.; Bai, Y.; Wierzbicki, T. J Solid Mech Mater Eng 2008, 2, 924.
25. Teng, X.; Mae, H.; Bai, Y.; Wierzbicki, T. Eng Fracture Mech 2008, 75, 4610.
26. Nicolopoulos, D.; Winkelmuller, G. Lect Notes Comput Sci 1996, 1067, 66.
27. Tai, H. Proc J SME Annu Meeting 2002, 5, 205.
28. Tai, H. IEIC Tech Report 2005, 100, 13.
29. Nicolopoulous, D.; Dominguez, A. Lect Notes Comput Sci 2008, 1823, 454.
30. http://www.altair.com
31. Murakami, D.; Kobayashi, S.; Torigaki, T.; Shizawa, K. Trans Jpn Soc Mech Eng A 2002, 68, 674.
32. Murakami, D.; Kobayashi, S.; Torigaki, T.; Shizawa, K. Trans Jpn Soc Mech Eng A 2002, 68, 682.
33. Kobayashi, S.; Tomii, D.; Shizawa, K. Trans Jpn Soc Mech Eng A 2004, 70, 810.
34. Mae, H.; Kishimoto, K. J Solid Mech Mater Eng 2007, 1, 35.
35. Steenbrink, A. C.; van der Giessen, E.; Wu, P. D. J Mech Phys Solids 1997, 45, 405.
36. Pijnenburg, K. G. W.; Seelig, T.; van der Giessen, E. Eur J Mech A/Solids 2005, 24, 740.
37. Zairi, F.; Nait-Abdelaziz, M.; Woznica, K.; Gloaguen, J. M. Eur J Mech A/Solids 2005, 24, 169.
38. Zairi, F.; Nait-Abdelaziz, M.; Gloaguen, J. M.; Lefebvre, J. M. Int J Plast 2008, 24, 945.
39. RADIOSS User's Code Interface Manual; Altair Engineering Inc, 2003.
40. Zhang, Z. L.; Hauge, M.; Odegard, J.; Thaulow, C. Int J Solids Struct 1999, 36, 2386.
41. Mae, H.; Kishimoto, K. Trans Soc Automot Eng Jpn 2007, 38, 63.
42. Bao, Y.; Wierzbicki, T. J Eng Mater Tech 2004, 126, 314.
43. Wierzbicki, T.; Bao, Y.; Lee, Y.-W.; Bai, Y. Int J Mech Sci 2005, 47, 719.
44. Teng, X.; Wierzbicki, T. Eng Frac Mech 2006, 73, 1653.
45. Rice, J. R.; Tracey, D. M. J Mech Phys Solids 1969, 17, 201.
46. Hancock, J. W.; Mackenzie, A. C. J Mech Phys Solids 1976, 24, 147.
47. Johnson, G. R.; Cook, W. H. Eng Fracture Mech 1985, 21, 31.
48. Barsoum, I.; Faleskog. J Int J Solids Struct 2007, 44, 1768.